Optical and SAR Image Registration Using Complexity Analysis and Binary Descriptor in Suburban Areas

Zhihua Xie, Jinghong Liu, Chenglong Liu, Yujia Zuo, and Xin Chen

***Abstract*— Optical and synthetic aperture radar (SAR) image registration is a challenging task due to significant geometric and radiometric differences. In particular, the strong scattering phenomenon in SAR images can seriously affect the registration results. Accordingly, to solve the low repeatability of the key points in optical and SAR images, a complexity analysis scheme is proposed. In the first phase, the complexity distribution diagram is calculated by the threshold sliding window in the edge images obtained from the maximum moment of the phase congruency. Then morphological operation and connected regions are used to obtain the high-complexity regions and mask them to avoid the extraction of the interference points. Next to solve the limitations of the local self-similarity (LSS) descriptor in the optical and SAR image registration, such as poor discrimination, expensive computational complexity, and sensitivity to large geometric and radiometric difference, we propose a binary LSS descriptor (BLSS). We replace the correlation surface of the LSS with the local gradient orientation histogram. Furthermore, we construct descriptors based on the *XY*-coordinate system and convert the correlation of the regions to binary descriptors. Finally, the fast sample consensus (FSC) is used to remove false correspondences. The experiments conducted on several optical and SAR image pairs verify the effectiveness of the proposed algorithm.**

***Index Terms*— Binary descriptor, complexity analysis, image registration, local self-similarity (LSS).**

I. Introduction

MULTISENSOR image registration plays a vital role in remote sensing image processing and is widely used in geological exploration, counterterrorism, data fusion, and other applications [1], [2]. Two operations are crucial for image registration tasks, namely, feature detection and descriptor construction. In particular, the considerable geometric and radiometric distortions for synthetic aperture radar (SAR) images create a bottleneck problem for aligning optical and SAR images.

At present, feature-based algorithms have undergone rapid development in remote sensing image registration. These algorithms can be composed of discriminative feature detectors and descriptors. First, there are many types of feature detectors, including Harris detector [3], Hessian detector [4], and others. Among them, the Harris detector is the most popular for multimodal image registration. However, it is vulnerable to noise and images with less structural information. Thus, some improved algorithms are proposed to optimize it. For example, since the Harris detector is sensitive to scale changes, Xiang *et al.* [5] proposed a multiscale Harris detector that can robustly tackle large-scale differences. To tackle the influence of speckle noise, Fan *et al.* [6] proposed a uniform nonlinear diffusion algorithm (UND-Harris). Furthermore, Ye *et al.* [7] proposed a novel key point detector by integrating both corners and blobs, which can improve key point repeatability and registration accuracy. However, these detectors are sensitive to the strong scattering phenomenon in SAR system. Hence, traditional algorithms are incapable of matching images with high-complexity regions.

Once key points are detected, feature descriptors are established for these key points. Commonly used descriptors are the scale-invariant feature transform (SIFT) [8] descriptor, the histogram of oriented gradients (HOGs) [9], the local binary patterns (LBPs) descriptor [10], the local self-similarity (LSS) descriptor [11], and others. However, the above traditional descriptors are not suitable for optical and SAR image registration because of the various differences between the optical and SAR images, including geometric differences, radiometric differences, the strong scattering phenomenon, and others. Hence, many descriptors have been proposed to overcome these problems. For example, Ye *et al.* [12] proposed the histogram of oriented phase congruency (HOPC) to address nonlinear radiometric differences. HOPC reflects the structural properties of images based on phase congruency (PC). However, HOPC is sensitive to scale and geometric changes. Paul and Pati [13] proposed a structural descriptor using PC to solve the geometric differences. Since the descriptor dimensions are comparatively high, complicated computations are needed. Ye *et al.* [14] improved the LSS descriptor by combining the LSS descriptors in several small regions to overcome the nonlinear intensity difference; however, this method is computationally expensive.

In summation, the key to the optical and SAR image registration is to improve key point repeatability and the robustness and efficiency of descriptors. We propose a method to solve

Manuscript received January 27, 2021; revised March 3, 2021 and March 25, 2021; accepted April 5, 2021. Date of publication April 21, 2021; date of current version December 29, 2021. This work was supported by the Jilin Scientific and Technological Development Program under Grant 20180201054SF. *(Corresponding author: Jinghong Liu.)*

Zhihua Xie and Xin Chen are with the Key Laboratory of Airborne Optical Imaging and Measurement, Changchun Institute of Optics, Fine Mechanics and Physics, Chinese Academy of Sciences, Changchun 130033, China, and also with the College of Materials Sciences and Opto-Electronic Technology, University of Chinese Academy of Sciences, Beijing 100049, China (e-mail: xiezhihua17@mails.ucas.ac.cn; chenxin176@mails.ucas.ac.cn).

Jinghong Liu, Chenglong Liu, and Yujia Zuo are with the Key Laboratory of Airborne Optical Imaging and Measurement, Changchun Institute of Optics, Fine Mechanics and Physics, Chinese Academy of Sciences, Changchun 130033, China (e-mail: liu1577@126.com; liuchenglong14@mails.ucas.ac.cn; mzyj0617@126.com).

Digital Object Identifier 10.1109/LGRS.2021.3071870

the low repeatability of key points in optical and SAR images caused by the high-complexity and strong scattering regions, which are collectively referred to as high-complexity regions; and improve the matching efficiency using a novel binary descriptor. Strong scattering is caused by the high-reflectivity regions where the metal target or dihedral target is located in SAR images, which do not exist in optical images. Thus, the imaging characteristics of these regions are quite different and difficult to match. In addition, we use the Harris detector to extract key points from the optical and SAR edge images. Furthermore, we use the Hamming distance and fast sample consensus (FSC) [15] to complete the matching process. The main contributions of this letter are as follows.

1) A novel method is proposed to identify high-complexity and strong scattering regions from optical and SAR edge images, which are obtained from the maximum moment of the PC. Then these regions are masked to avoid processing and reduce the extraction of interference points.
2) A binary LSS descriptor (BLSS), is developed based on the local gradient orientation histogram to address the complicated computations and geometric and radiometric differences between optical and SAR images.

The remainder of this letter is organized as follows. Section II describes the complexity analysis method and the novel BLSS. Section III analyzes the performance of the proposed algorithm. Section IV presents the conclusion and recommendations for future study.

II. Methodology

This section first introduces the complexity analysis method and then illustrates the novel binary descriptor design process.

A. Complexity Analysis Method

Due to the large intensity differences between the optical and SAR images, we use the maximum moment of the PC [16] to extract the edge information. In addition, we found that the edge information of the high-complexity regions in high-resolution SAR images is inconsistent with the corresponding regions in optical images. As Fig. 1 shows, the regions marked with red and green lines have high complexity. A comparison of Fig. 1(c) and (f) corresponding to the regions marked with red lines shows that there is no consistency of the edge information, and it is easy to extract more corner points whose surrounding information is disorganized. Thus, the descriptors are not representative and cannot be matched. These key points, called inference points, can increase the computation and lower their repeatability in optical and SAR images.

Accordingly, this letter proposes a complexity analysis method based on edge images to avoid the extraction of interference points from high-complexity regions and improve key point repeatability. In this method, the binary image $f(i, j)$ is generated from the edge image $I(i, j)$

$$f(i,j) = \begin{cases} 1, & I(i,j) \neq 0 \\ 0, & I(i,j) = 0. \end{cases} \tag{1}$$

Then a $N \times N$ nonoverlapping sliding window is moved over the binary image. To prevent the misjudgment of the high-complexity regions when sliding along the edge orientation, we count the intensity values $f(i, j)$ in four orientations with $\theta = \{0°, 90°, 180°, \text{and } 270°\}$ and obtain the complexity distribution diagram $f'_\theta(x, y)$ in the single orientation θ and the final complexity distribution diagram $B(x, y)$

$$f'_\theta(x,y) = \sum_{(i,j)\in N} f_\theta(i,j), \quad ((x,y) \in \text{round}((i,j)/N)) \tag{2}$$

$$B(x,y) = \begin{cases} 1, & \prod_{\theta=1}^{4} f'_\theta(x,y) \geq T_m \\ 0, & \prod_{\theta=1}^{4} f'_\theta(x,y) < T_m \end{cases} \tag{3}$$

where the size of the sliding window is $N = 5$ and the threshold $T_m = 13$. The resulting edge complexity is shown in Fig. 2.

Fig. 2 shows that the upper left region corresponds to the high-complexity region. Furthermore, Fig. 3 shows that there

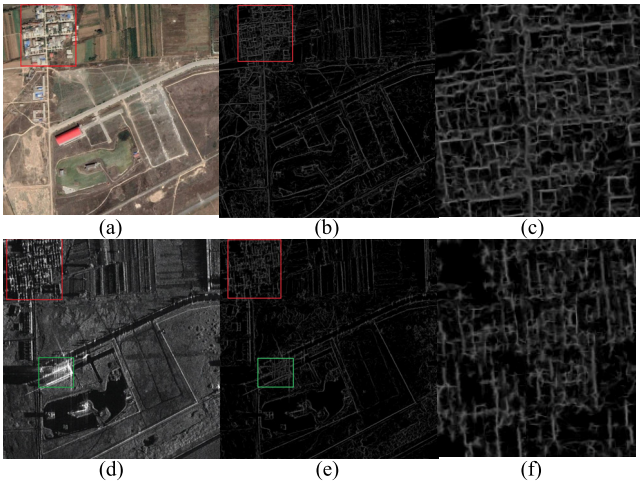

Fig. 1. Comparison of optical and SAR images. (a) Optical image. (b) Optical edge image. (c) Enlarged view of the red line marked region in (b). (d) SAR image. (e) SAR edge image. (f) Enlarged view of the red line marked region in (e).

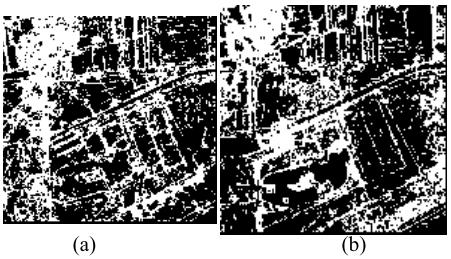

Fig. 2. Diagram of complexity distribution. (a) Optical image. (b) SAR image.

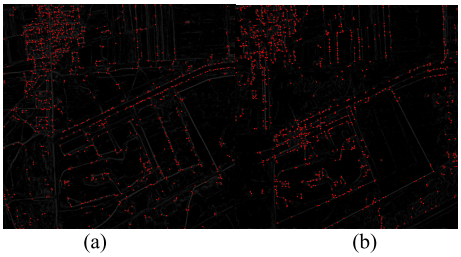

Fig. 3. Key points on two edge images. (a) Optical image. (b) SAR image.

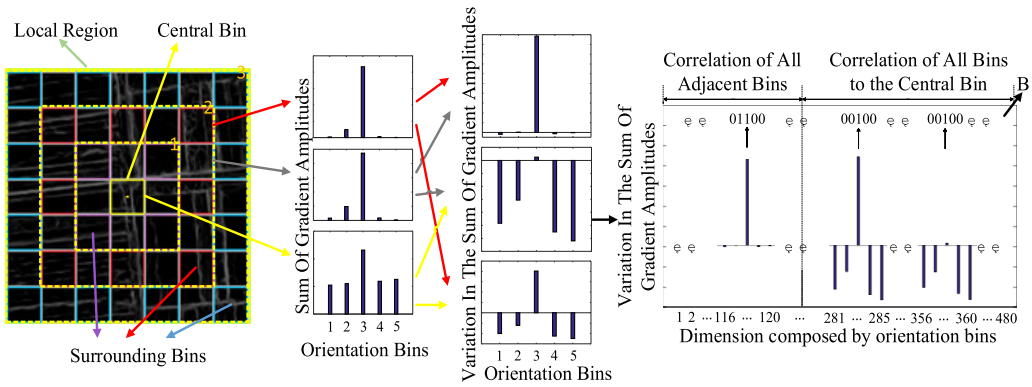

Fig. 4. Schemes of the BLSS descriptor computation.

TABLE I
COMPARISONS ON REPEATABILITY RATES

Parameters	P-A		P-B	
	NCA	CA	NCA	CA
γ (%)	10.64	14.45	12.26	16.01

are many interference points in the corresponding region. Once the complexity distribution diagram is obtained, by combining the "open operation" (a basic morphological operation) with the four connected regions methods, the high-complexity regions are obtained and masked to avoid extracting key points from this region. Here we extract key points from edge images using the Harris detector. Table I shows the repeatability rate γ between optical and SAR images, to the method with complexity analysis (CA) and the method without complexity analysis (NCA). The threshold between repeatable key points is set to 2. Table I shows that CA gains approximately 4% points compared with NCA. Therefore, CA can improve the key point repeatability rate. As shown, the two methods have low repeatability on the optical and SAR images because of serious nonlinear radiometric differences, which means that the optical and SAR image registration is a challenging task.

B. Construction Method of BLSS Descriptor

Since the LSS descriptor calculates the self-similarity in a single orientation, it cannot provide enough discriminability, and the initial correspondences between optical and SAR images may have many-to-one cases. Therefore, this letter proposes a BLSS descriptor based on edge images to highlight the structural characteristics of optical and SAR images. The region around a key point is divided into small bins, and the structural characteristics in each bin are described by the local gradient orientation histogram instead of the correlation surface in LSS to improve descriptor determination. Additionally, the correlation between small bins is mapped into binary mode to improve algorithm efficiency. The BLSS descriptor construction process is illustrated in Fig. 4.

In detail, before the BLSS, we first compute the gradient magnitude $D(X_i)$ and orientation $\theta(X_i)$ of pix X_i from edge images based on the XY-coordinate system. They are computed as follows:

$$D(X_i) = \sqrt{D_x(X_i)^2 + D_y(X_i)^2} \tag{4}$$

$$\theta(X_i) = \tan^{-1}\big(D_y(X_i)/D_x(X_i)\big). \tag{5}$$

Then we normalize them to $[0 \sim 1)$ and $[0° \sim 180°)$, respectively. All small bins are divided into three circles; and there are 8, 16, and 24 bins in each circle, respectively. We obtain the statistics of the gradient orientation histogram of each bin as a self-similarity vector. Generally, angles ranging from 0° to 180° are divided into eight orientation bins. However, it is unsuitable for our proposed descriptor. We compress the eight orientation bins to five orientation bins, which can reduce the dimensionality of the descriptor and solve the problem that the binary descriptor is sensitive to orientation information. The compression method converts the middle six orientation bins into three orientation bins. In this way, large values can be obtained on the dimension, which makes the structural characteristics more significant.

For each bin, we define the statistic of the gradient orientation histogram in five orientations as a vector $d_{i,j}$. The variations between adjacent bins in each circle are calculated as a self-similarity vector D_{Adjace}, which is given by

$$D_{\text{Adjace}} = \{\Delta d_{1,1}, \ldots, \Delta d_{1,8}, \Delta d_{2,1}, \ldots, \Delta d_{2,16}, \Delta d_{3,1}, \ldots, \Delta d_{3,24}\} \tag{6}$$

where $d_{i,j}$ represents the vector corresponding to the jth bin of the ith circle calculated by the gradient orientation histogram. $\Delta d_{i,j}$ is given by

$$\Delta d_{i,j} = \begin{cases} d_{i,j+1} - d_{i,j}, & i = 1,2,3 \;\; j = 1,2,\ldots,8\times i - 1 \\ d_{i,1} - d_{i,8\times i}, & i = 1,2,3 \;\; j = 8\times i. \end{cases} \tag{7}$$

Then the variations between the surrounding bins and the center bin are calculated as another self-similarity vector D_{Central}, which is given by

$$D_{\text{Central}} = \{\Delta d'_{1,1}, \ldots, \Delta d'_{1,8}, \Delta d'_{2,1}, \ldots, \Delta d'_{2,16}, \Delta d'_{3,1}, \ldots \Delta d'_{3,24}\} \tag{8}$$

$$\Delta d'_{i,j} = d_{i,j} - d_{0,0}, \quad i = 1,2,3 \;\; j = 1,2,\ldots,8\times i \tag{9}$$

where $d_{0,0}$ represents the vector of the center bin calculated by the local gradient orientation histogram.

Finally, the above self-similarity vectors are concatenated to obtain $\{D_{\text{Adjace}}, D_{\text{Central}}\}$. Because the positive and negative elements in the self-similarity vectors reflect the variation tendency of the structural characteristics in each orientation, we convert the positive and negative elements into the binary modes 1 and 0 to obtain the final descriptor B.

The sorting rules of neighbor bins are as follows: First, the main orientation bin of the support region bin_0 is calculated. Then the starting bin in each circle is calculated by $\text{bin}_0 \times i (i = 1, 2, 3)$ and sorted in counterclockwise order.

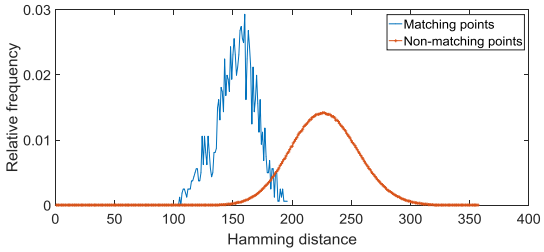

Fig. 5. Distributions of Hamming distances for matching correspondences and nonmatching correspondences.

Fig. 5 evaluates the performance of our descriptor. We use the distribution of the Hamming distance to evaluate our descriptor. We extract approximately 2500 correspondences from Pair A in Section III and exhibit the distributions of the Hamming distances between matching points and nonmatching points in Fig. 5. Since the dimensionality of our binary descriptor is 480, the maximum possible Hamming distance is 480 bits. As Fig. 5 shows, the distribution of the Hamming distances for nonmatching points is roughly Gaussian and centered around a larger value than the matching points overtly. There are large geometric and radiometric differences between optical and SAR images, so the Hamming distance of matching correspondences does not start from a very small value such as binary robust independent elementary features (BRIEF) [17]. However, the distance between the expectations of the two curves is relatively large. This indicates that the Hamming distance between matching and nonmatching correspondences is obvious and separable. Therefore, our descriptor is discriminative and robust.

Additionally, we compare the running time of LSS and the proposed BLSS descriptor under similar numbers of key points. The average running times of LSS and BLSS are 17.8098 and 8.7035 s, respectively. This means that BLSS is superior to LSS in computational efficiency. In addition, the Hamming distance is used to measure the similarity of descriptors in our algorithm, and outliers are removed by FSC to obtain the final matching pairs for optical and SAR images. Finally, we use the affine transformation to rectify the sensed image.

III. Experiments

This section evaluates the capability of the proposed algorithm with optical and SAR images. The optical-to-SAR SIFT method (OS-SIFT) [5], radiation-variation insensitive feature transform method (RIFT) [18], and robust optical and SAR image registration based on PC method (ROS-PC) [19] algorithms are used for comparison. ROS-PC is an improvement of RIFT, and the three algorithms show good performances for optical and SAR image registration. Their implementation was obtained from the authors' personal websites. Note that our test images are based on geographic coordinates, so there are no large rotational differences between optical and SAR images. All experiments were conducted using the MATLAB R2016a software.

A. Parameter Settings

In our experiments, the sizes of the "open operation" templates are set to 9×9 and 6×6 to partition the complexity regions in optical and SAR images. The key point detection thresholds are both set between 0.02 and 0.08, and we empirically select a larger radius of 91 pix for the support region around a key point to obtain more information. The parameter settings of the two state-of-the-art comparative algorithms follow their authors' instructions, and we fine-tuned the detection thresholds to obtain similar numbers of key points.

TABLE II
Details of the Test Images

Pair	Image source	Resolution	Date	Size
A	Google Earth	1 m	2020/7/25	1201 × 1219
A	Airborne SAR	1 m	2019/11/5	1211 × 1238
B	Google Earth	3 m	2020/7/25	1739 × 1060
B	Airborne SAR	3 m	2019/11/5	1768 × 1078
C	Google Earth	3 m	2020/7/25	2002 × 1251
C	Airborne SAR	3 m	2019/11/5	1689 × 1143

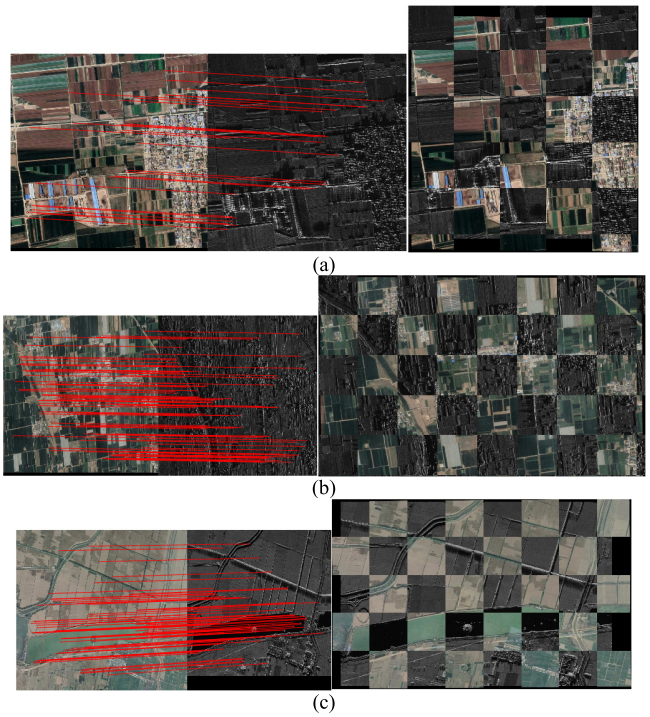

Fig. 6. Registration and check board fusion results of the proposed method. (a) Pair A. (b) Pair B. (c) Pair C.

B. Registration Performance of the Proposed Algorithm

The performance is evaluated using three optical and SAR image pairs that have significant imaging differences. Table II shows the details of the three test image pairs. Fig. 6 shows the matching and checkerboard fusion results for a visual check.

All three image pairs describe suburban areas with significant geometric and radiometric differences. Especially for Pairs A and B, it is a challenging task since there are many roofs in the images. The side-looking mechanism of airborne SAR sensors causes roof areas to suffer from strong scattering and shadows, which do not exist in the corresponding optical images. However, Fig. 6 shows that the matching points of the three image pairs are all located in the correct positions, and the checkerboard fusion results are satisfactory.

TABLE III
CMNS AND RMSES OF SEVERAL METHODS FOR TEST IMAGES

Method	P-A		P-B		P-C	
	CMN	RMSE	CMN	RMSE	CMN	RMSE
OS-SIFT	6	8.2847	*	*	8	6.7871
RIFT	*	*	57	6.9979	66	7.8074
ROS-PC	*	*	67	6.1316	73	5.3423
Proposed	26	2.7718	81	4.0623	78	3.7548

*: Fails to register the image pair (CMN<3)

C. Experiment Analysis

The correct matching number (CMN) and the root-mean-square error (RMSE) are used to evaluate the performance of the above methods. CMN is obtained by removing outliers from the initial matches using FSC. RMSE is computed as follows:

$$\mathrm{RMSE} = \sqrt{\frac{1}{m}\sum_{i=1}^{m}\left[\left(x_i^{o_1} - x_i^s\right)^2 + \left(y_i^{o_1} - y_i^s\right)^2\right]}. \quad (10)$$

Twenty checkpoints are manually selected from optical and SAR images to estimate the affine transformation matrix H. (x_i^o, y_i^o) and (x_i^s, y_i^s) are the coordinates of the ith correspondence after FSC. $(x_i^{o_1}, y_i^{o_1})$ denotes the transformed coordinates of (x_i^o, y_i^o) by H, and m is the number of the correspondences after FSC.

Table III shows the quantitative results of the four methods. For Pair A, RIFT and ROS-PC fail to register the images because the highly complex regions in the images can reduce the number of repeatable key points, and the PC information in these regions varies greatly. RIFT and ROS-PC, both use PC to describe the structural information, and the descriptors can be seriously affected by the disorganized PC information in these regions. Although several correct correspondences are obtained by OS-SIFT, the CMN and RMSE are obviously inferior compared to those of the proposed method. This is due to the complexity analysis scheme of the proposed method. For Pair B with strong radiometric differences, there is rich structural information, and there are fewer high-complexity regions than Pair A. OS-SIFT fails to correctly register the images due to the obvious gradient difference and scattering in the SAR image. RIFT performs better than OS-SIFT since it uses PC to capture structural information. ROS-PC has a larger CMN and smaller RMSE than RIFT since its descriptor is constructed using multiscale features, which make it more robust. Although the RMSE of the proposed method is above 4 pix, it is superior to ROS-PC in both the CMN and RMSE. The BLSS descriptor is based on the self-similarity of the PC information, so it can better overcome the strong radiometric difference. For Pair C, there are small geometric and radiometric differences between the optical and SAR images, and the proposed method achieves the largest CMN and smallest RMSE, benefiting from the robust feature detector and the discriminative BLSS descriptor, both based on the maximum moment of PC. Note that the RMSEs in Table III are relatively large due to the high-resolution images with significant nonlinear distortions. The affine transformation used cannot effectively address these distortions. However, the experimental results demonstrate that our method gives the best performance among the four methods.

IV. CONCLUSION

In this letter, a complexity analysis scheme is proposed to improve the key point repeatability of the optical and SAR images. Furthermore, a novel binary descriptor generation method is proposed for optical and SAR images with geometric and radiometric differences. The experimental results show that our algorithm achieves comparable performance to solve the large geometric and radiometric differences and notably improves the matching accuracy. Our algorithm can be used for optical and SAR image registration with geographic information encoding. The limitations are that it is sensitive to rotation invariance, and the matching accuracy is not quite satisfactory. We will employ the rotation invariance of descriptors and improve the accuracy in the future works.

REFERENCES

[1] J. Li, Q. Hu, and M. Ai, "Robust feature matching for remote sensing image registration based on L_q-estimator," *IEEE Geosci. Remote Sens. Lett.*, vol. 13, no. 12, pp. 1989–1993, Dec. 2016.
[2] Y. Ye, L. Bruzzone, J. Shan, F. Bovolo, and Q. Zhu, "Fast and robust matching for multimodal remote sensing image registration," *IEEE Trans. Geosci. Remote Sens.*, vol. 57, no. 11, pp. 9059–9070, Nov. 2019.
[3] C. Harris and M. Stephens, "A combined corner and edge detector," in *Proc. Alvey Vis. Conf.*, Manchester, U.K., 1988, pp. 147–151.
[4] P. R. Beaudet, "Rotationally invariant image operators," in *Proc. Int. Joint Conf. Pattern Recognit.*, 1978, pp. 579–583.
[5] Y. Xiang, F. Wang, and H. You, "OS-SIFT: A robust SIFT-like algorithm for high-resolution optical-to-SAR image registration in suburban areas," *IEEE Trans. Geosci. Remote Sens.*, vol. 56, no. 6, pp. 3078–3090, Jun. 2018.
[6] J. Fan, Y. Wu, M. Li, W. Liang, and Y. Cao, "SAR and optical image registration using nonlinear diffusion and phase congruency structural descriptor," *IEEE Trans. Geosci. Remote Sens.*, vol. 56, no. 9, pp. 5368–5379, Sep. 2018.
[7] Y. Ye, M. Wang, S. Hao, and Q. Zhu, "A novel keypoint detector combining corners and blobs for remote sensing image registration," *IEEE Geosci. Remote Sens. Lett.*, vol. 18, no. 3, pp. 451–455, Mar. 2021.
[8] D. G. Lowe, "Distinctive image features from scale-invariant keypoints," *Int. J. Comput. Vis.*, vol. 60, no. 2, pp. 91–110, Nov. 2004.
[9] N. Dalal and B. Triggs, "Histograms of oriented gradients for human detection," in *Proc. IEEE Comput. Soc. Conf. Comput. Vis. Pattern Recognit. (CVPR)*, Jun. 2005, pp. 886–893.
[10] Z. Guo, L. Zhang, and D. Zhang, "A completed modeling of local binary pattern operator for texture classification," *IEEE Trans. Image Process.*, vol. 19, no. 6, pp. 1657–1663, Jun. 2010.
[11] E. Shechtman and M. Irani, "Matching local self-similarities across images and videos," in *Proc. IEEE Conf. Comput. Vis. Pattern Recognit.*, Jun. 2007, pp. 1–8.
[12] Y. Ye, J. Shan, L. Bruzzone, and L. Shen, "Robust registration of multimodal remote sensing images based on structural similarity," *IEEE Trans. Geosci. Remote Sens.*, vol. 55, no. 5, pp. 2941–2958, May 2017.
[13] S. Paul and U. Pati, "Automatic optical-to-SAR image registration using a structural descriptor," *IET Image Process.*, vol. 14, no. 1, pp. 62–73, Jan. 2020.
[14] Y. Ye, L. Shen, M. Hao, J. Wang, and Z. Xu, "Robust optical-to-SAR image matching based on shape properties," *IEEE Geosci. Remote Sens. Lett.*, vol. 14, no. 4, pp. 564–568, Apr. 2017.
[15] Y. Wu, W. Ma, M. Gong, L. Su, and L. Jiao, "A novel point-matching algorithm based on fast sample consensus for image registration," *IEEE Geosci. Remote Sens. Lett.*, vol. 12, no. 1, pp. 43–47, Jan. 2015.
[16] P. Kovesi, "Phase congruency: A low-level image invariant," *Psychol. Res.*, vol. 64, no. 2, pp. 136–148, Dec. 2000.
[17] M. Calonder, V. Lepetit, C. Strecha, and P. Fua, "BRIEF: Binary robust independent elementary features," in *Proc. Eur. Conf. Comput. Vis.*, vol. 6314, 2010, pp. 778–792.
[18] J. Li, Q. Hu, and M. Ai, "RIFT: Multi-modal image matching based on radiation-variation insensitive feature transform," *IEEE Trans. Image Process.*, vol. 29, pp. 3296–3310, Dec. 2020.
[19] L. Wang, M. Sun, J. Liu, L. Cao, and G. Ma, "A robust algorithm based on phase congruency for optical and SAR image registration in suburban areas," *Remote Sens.*, vol. 12, no. 20, p. 3339, Oct. 2020.